Observing the dynamics of dipole-mediated energy transport by interaction enhanced imaging

G. Günter,[1] H. Schempp,[1] M. Robert-de-Saint-Vincent,[1] V. Gavryusev,[1]
S. Helmrich,[1] C. S. Hofmann,[1] S. Whitlock [1†] and M. Weidemüller [1*‡]

[1]Physikalisches Institut, Universität Heidelberg,
Im Neuenheimer Feld 226, 69120, Heidelberg, Germany

[‡] Also at: University of Science and Technology of China, Hefei, Anhui 230026, China
[†] E-mail: whitlock@physi.uni-heidelberg.de
[*] E-mail: weidemueller@uni-heidelberg.de

Electronically highly excited (Rydberg) atoms experience quantum-state changing interactions similar to Förster processes found in complex molecules, offering a model system to study the nature of dipole-mediated energy transport under the influence of a controlled environment. We demonstrate a non-destructive imaging method to monitor the migration of electronic excitations with high time and spatial resolution using electromagnetically induced transparency on a background gas acting as an amplifier. The many-body dynamics of the energy transport is determined by the continuous spatial projection of the electronic quantum state under observation and features an emergent spatial scale of micrometer size induced by Rydberg-Rydberg interactions.

Watching a many-body quantum system evolve under the influence of well controlled interactions is the basic essence of Feynman's vision for a quantum simulator (*1–3*), which could be used to address fundamental questions about coherent-quantum and open-system dynamics in diverse settings (*4, 5*). One such question is the nature of energy transfer in real physical systems, such as complex chemical reactions, excitonic transport in organic semiconductors (*6*) and molecular aggregates (*7*) or photosynthetic light-harvesting complexes (*8*). Both disorder and environment play crucial roles in the transport dynamics. In particular, it is unclear to which extent quantum-mechanical effects may enhance or reduce its efficiency (*9*).

The simulation of random walks in the quantum regime has recently been rendered accessible using manipulation techniques for single atoms (*10, 11*) and photons (*12*). In order to

study dipole-induced energy transport in a many-body environment, ultracold gases of highly-excited (Rydberg) atoms, which possess exceptionally large dipole moments and long-range quantum-state changing interactions, represent a unique model system (*13, 14*). Evidence of Rydberg energy exchange has been deduced from spectroscopic properties of optical Rydberg excitation (*15–18*), and from the macroscopic transfer of Rydberg state populations (*19, 20*). So far however, the direct microscopic observation of Rydberg energy transport has remained out of reach due to the difficulty in spatially following the migration of Rydberg excitations in real time. The first images of Rydberg atoms have recently been obtained using destructive methods such as field-ion microscopy (*21*), optical pumping of Rydberg atoms back to the ground state followed by high resolution fluorescence imaging (*22*), or core electron absorption in two-electron Rydberg-atoms (*23*). Here, we realize a non-destructive and state-selective optical imaging technique, as proposed in (*24, 25*), which is particulary adapted to investigate Rydberg energy transport under continuous observation. Each Rydberg impurity locally triggers strong absorption by many neighbouring background atoms, allowing one to image small numbers of otherwise invisible impurities. We observe and control transport dynamics on micrometer length scales with microsecond resolution. We show that the dynamics are affected by the back-action of the continuous non-destructive measurement process which induces a transition to quasi-classical diffusive transport. Furthermore, the Rydberg blockade effect, in which the presence of a single Rydberg atom strongly suppresses subsequent excitation of additional atoms (*13*), introduces a characteristic length scale to the transport dynamics reminiscent of self-assembling systems.

The basic idea of our imaging method (*24*) is to exploit the strong interactions between impurity atoms in the Rydberg state $|i\rangle$ with a bath of surrounding atoms, each optically coupled to a probe Rydberg state $|p\rangle$. Impurity-probe interactions cause a level shift of the $|p\rangle$ states in the vicinity of each impurity, which is mapped onto the light field using an electromagnetically induced transparency (EIT) resonance (*26–28*). By recording the probe laser transmission on a charge coupled device (CCD) camera an absorption image of the distribution of impurities is produced (Fig. 1A). The ultracold atomic gas is dressed by a strong coupling laser field (with Rabi frequency Ω_c) and a weaker probe laser field (Ω_p). The intermediate state $|e\rangle$ is short lived with a spontaneous scattering rate Γ. Destructive interference between excitation pathways decouples the atoms from the probe laser (*29*), except in the vicinity of an impurity atom where the EIT condition is broken causing the surrounding probe atoms to become strongly absorbing.

The radius of the absorbing spot around each impurity is given by the interstate-blockade radius R_{ip}, corresponding to the distance at which the EIT spectral half width ($\Omega_c^2/2\Gamma$ in the weak probe limit neglecting laser linewidths) equals the interaction induced level shift (Fig. 1B). Thus, each impurity is effectively accompanied by a sphere of absorbing atoms which enables us to monitor its location and dynamics. Strong impurity-probe interactions are achieved using resonant Rydberg-Rydberg interactions (Förster resonance) (*13*). The Rydberg blockade introduces another important length scale to the system, the impurity-impurity blockade radius R_{ii}, which is the closest distance between two impurities after laser excitation. By choosing appropriate states or by using modest electric fields to tune the Förster resonance it is possible

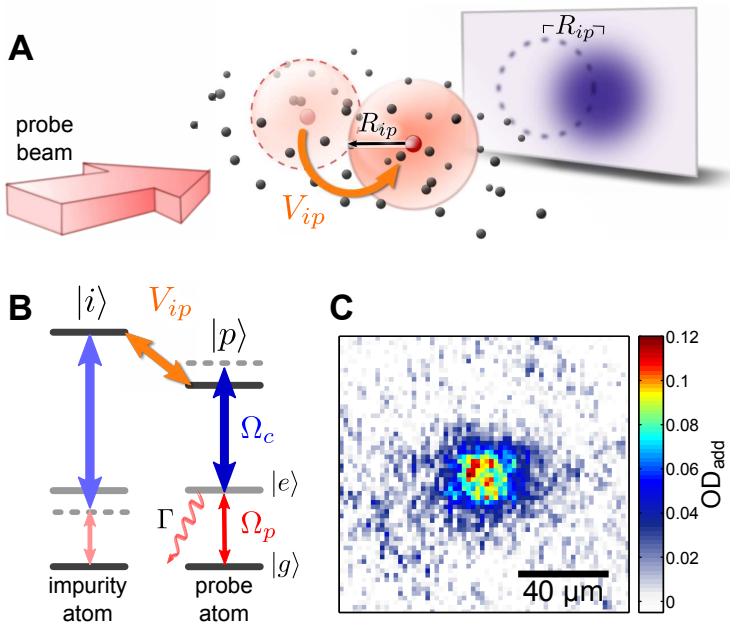

Figure 1: **Interaction enhanced imaging scheme for studying transport dynamics**. (**A**) Each impurity (red dot) breaks the EIT-condition for probe atoms within a volume characterized by R_{ip} due to the interaction induced level-shift on an auxiliary Rydberg-state $|p\rangle$ of the probe atoms. These atoms therefore strongly absorb the probe beam, casting a shadow in the images. State exchange interactions with strength V_{ip} lead to impurity transport. (**B**) Simplified level diagram showing the involved states in the excitation of the Rydberg-impurities $|i\rangle$ as well as the states involved in the EIT-ladder scheme, which is used to probe the level-shift on the state $|p\rangle$. (**C**) Averaged optical density image of an impurity distribution for approximately 100 impurities.

to independently vary R_{ii} and R_{ip}.

To demonstrate the essential features of the imaging method, Rydberg impurities in state $|i = 50S\rangle$ are excited in a small central region of the cloud (*30*). The excitation pulse is followed by the acquisition of the probe absorption image under EIT-conditions using separate lasers which couple to the probe state $|p = 37S\rangle$. For weak enough probe light, blockade effects between the probe atoms, which would lead to a reduced transparency, can be neglected (*24*). From comparison with an image without impurities we determine the additional optical density $\mathrm{OD_{add}}$ due to the presence of impurities, from which we extract the number of additional two-level absorbers N_{add}. A typical image of approximately 100 impurity atoms (averaged over 100 shots) is shown in Fig. 1C. In Fig. 2 we show the number of additional absorbers as a function of the number of impurity atoms N_{imp} measured by field-ionization detection. For low numbers of impurities, a linear dependence is observed as each impurity blocks roughly the same number of probe atoms. From the slope, we determine an amplification factor of $A = N_{add}/N_{imp} = 19 \pm 2$.

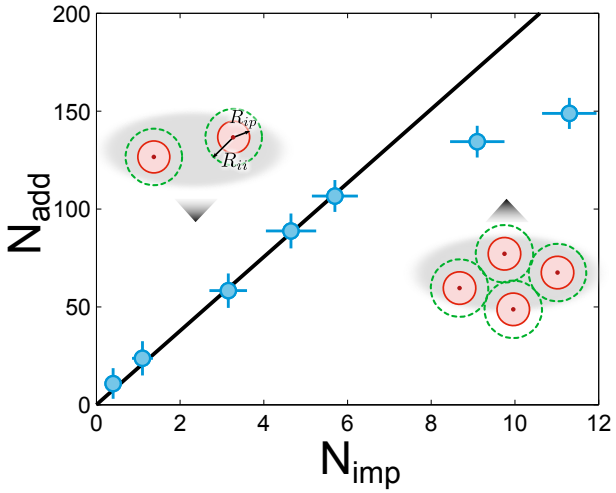

Figure 2: **Dependence of the number of additional absorbers on the number of impurities**. For small numbers of impurities the number of additional absorbers grows linearly. The black line is a fit used to determine the amplification factor. For high impurity numbers the additional absorbers and the blockaded fraction saturate due to the Rydberg blockade effect. In this regime the additional impurities are only excited in the low density wings of the cloud, therefore not significantly increasing the number of additional absorbers.

The optical depth per interstate blockade sphere is $\mathrm{OD_{bl}} \approx 0.5$, suggesting that our images might be sensitive to single impurities. At present, however, we are limited by our optical resolution which is larger than both R_{ip} and R_{ii}, allowing us to clearly detect as few as 5 impurities in a single shot with $\lesssim 5\,\mu$s time-resolution. By improving the optical resolution below R_{ip} it will ultimately be possible to follow the evolution of individual impurities in real time. For increasing numbers of impurities (~ 10) we observe a saturation of the number of additional absorbers as shown in Fig. 2. This is a manifestation of the Rydberg blockade effect resulting in a saturation of the density of impurities. For stronger excitation the number of impurities increases further due to excitation in the low density wings of the cloud, but the number of additional absorbers is not significantly increased.

In order to study transport of the kind

$$|i\rangle \otimes |p\rangle \rightleftarrows |p\rangle \otimes |i\rangle \,, \tag{1}$$

we switch to states which possess strong dipolar state-exchange interactions. The effects of the Rydberg blockade and the continuous optical observation lead to interesting new features. In particular, the spatial correlations due to the Rydberg blockade and the dissipation induced by the scattering of probe light, which acts as a controlled environment, have a strong impact on the intrinsically coherent transfer mechanism. In a simplified picture, we consider coherent state exchange of an atom in state $|i\rangle$ with all of the surrounding atoms. The hopping frequency $\omega_{hop}(r) \simeq 2\rho_{pp}(r)V_{dd}(r)$ between an impurity and an atom at distance r depends on

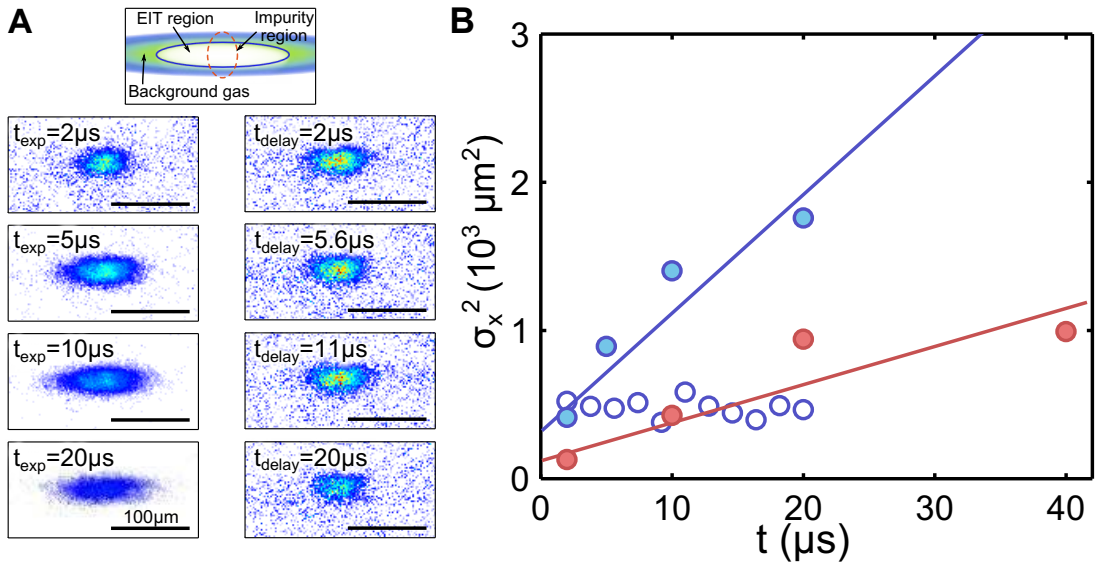

Figure 3: **Diffusion of Rydberg-impurities**. (**A**) The strong exchange interactions between impurities and probe atoms lead to an expansion of the Rydberg distribution in time in the presence of the imaging light. The top sketch shows the experimental geometry, while the following images show the additional optical depth for different exposure times (left column) or different delay times (right column), with fixed color scale (on the Förster resonance). (**B**) The squared-width of the distribution σ_x^2 increases approximately linearly with time. On the Förster resonance (full blue circles) the expansion is faster than off resonance (full red circles). For comparison, open blue circles show σ_x^2 on resonance for fixed exposure time (2 μs), but with varying delay between the excitation and the illumination of the atoms with imaging light..

the dipole-dipole exchange interaction $V_{dd}(r) = C_3/r^3$ and on the population $\rho_{pp}(r)$ of the $|p\rangle$ state. Through the dependence of ρ_{pp} on the laser fields and the blockade effect, it is possible to control the hopping dynamics. Light scattering by probe atoms causes a measurement-induced environmental decoherence rate $\gamma_{env} \simeq A\,\Omega_p^2/\Gamma$. Through the density and Ω_p this can be controlled independently of ω_{hop}. For our parameters we estimate that γ_{env} is typically 150 times higher than the peak value of $\omega_{hop}(r)$. Therefore we expect classical hopping to dominate with a rate $\Gamma_{hop}(r) \simeq \omega_{hop}^2(r)/\gamma_{env}$ to each of the neighbouring atoms. Due to the competition between the interstate Rydberg blockade and the $1/r^3$ scaling of V_{dd} there is a preferred hopping distance $r_{hop} \sim R_{ip}$. This introduces an intrinsic scale into the transport dynamics, similar to that of self-assembled systems. We expect the width of the impurity distribution in each direction $\sigma(t)$ to grow as $\sigma^2(t) = \sigma^2(0) + 2Dt$, with $D \simeq 5/18\,R_{ip}^2\,\Omega_p^2/\Gamma$ (see supplementary online text).

To investigate these dynamics we excite impurities in the $|i = 38S\rangle$ state and perform EIT with the $|p = 37S\rangle$ state. The pair state $|38S\rangle \otimes |37S\rangle$ couples to the exchange-symmetric pair-state $|37P\rangle \otimes |37P\rangle$. Therefore energy transport can occur due to $|38S\rangle \rightleftarrows |37S\rangle$ exchange. The

coupling $C_3 = 2\pi \times 1.6$ GHz μm^3 gives $R_{ip} = 6.3 \pm 0.5\,\mu$m. Figure 3A (left column) shows images of the impurity distribution for different exposure times. The distribution is seen to expand horizontally as a function of imaging exposure time. Expansion in the vertical direction is not observed due to the smaller size of the EIT coupling beam in this direction. In addition to the growing width, we observe a slight decay of N_{add} which can be attributed to the lifetime of the $|38S\rangle$ Rydberg state ($\approx 30\,\mu$s). To perform a quantitative analysis of the dynamics, we extract the second central moment σ_x^2 of the imaged distributions as a function of the exposure time. As shown in Fig. 3B for different conditions, σ_x^2 grows approximately linearly. On the Förster resonance and including the effect of time integration during the exposure pulse (see Material and Methods), we find $D = 80 \pm 13\,\mu\mathrm{m}^2/\mu$s. From the simple scaling discussed above we expect $D_{\mathrm{expect}} = 55 \pm 23\,\mu\mathrm{m}^2/\mu$s which agrees with the measurements.

To verify the role of the environment on the observed dynamics we also record images with a fixed short exposure time of $2\,\mu$s (Fig. 3A right column), but with different times between impurity excitation and image acquisition (while $\Omega_p = 0$). Here we observe no diffusion confirming that impurity-probe interactions are responsible for the dynamics, and that the dynamics can indeed be controlled by modifying the environment via the laser fields. Additionally this demonstrates that mechanical forces between impurity atoms do not play a significant role.

Finally we study transport in the regime of off-resonant exchange interactions. Earlier experiments under these conditions observed spectral broadening and rapid dephasing of coherent state transfer (*15–17*), which was too high to be explained by the process in eq. (1) alone. This was attributed to secondary processes resulting in enhanced spatial diffusion which we can now directly observe. By setting the electric field to zero we tune the Förster-defect to 100 MHz. Here, we expect weaker impurity-probe exchange interactions and a change in the character of the interactions to van der Waals type ($1/r^6$ scaling), resulting in a significantly smaller r_{hop}. In this case we measure slower diffusion with $D = 26 \pm 6\,\mu\mathrm{m}^2/\mu$s (Fig. 3B). However, this still is almost an order of magnitude faster than can be expected from the above model, including the slightly different experimental parameters (see supplementary online text). Our observation thus reveals that the diffusion involves additional processes (such as the always resonant secondary process $|37S\rangle \otimes |37P\rangle \rightleftarrows |37P\rangle \otimes |37S\rangle$), and that spatial diffusion of secondary $|nP\rangle$ excitations plays an important role for Rydberg-state dynamics and energy transfer.

In future work it may be possible to investigate the transition to coherent-quantum dynamics in many-body systems. By detuning the EIT lasers from the intermediate state, decoherence via photon scattering can be suppressed, while maintaining the preferred distance for hopping given by the blockade radius. This will allow for the study of excitonic behaviour, in which impurities evolve as delocalised superposition states. In this regime, transport should be completely different, leading to localisation or enhanced transport which can be controlled through the dimensionality, degree of disorder and dissipation in the system. By switching back to resonant probing this evolution could be observed. This provides an ideal platform for benchmarking current theories used to explain energy transport in complex systems such as light harvesting complexes, where for example the competition between mechanical and excitonic transport and the role of interactions are still open questions (*8*).

References and Notes

1. R. Feynman, *International Journal of Theoretical Physics* **21**, 467 (1982).
2. I. Bloch, J. Dalibard, S. Nascimbène, *Nature Physics* **8**, 267 (2012).
3. J. I. Cirac, P. Zoller, *Nature Physics* **8**, 264 (2012).
4. J. T. Barreiro, *et al.*, *Nature* **470**, 486 (2011).
5. H. Weimer, M. Müller, I. Lesanovsky, P. Zoller, H. P. Büchler, *Nature Physics* **6**, 382 (2010).
6. H. Najafov, B. Lee, Q. Zhou, L. Feldman, V. Podzorov, *Nature materials* **9**, 938 (2010).
7. A. M. van Oijen, M. Ketelaars, J. Köhler, T. J. Aartsma, J. Schmidt, *Science* **285**, 400 (1999).
8. E. Collini, *Chem. Soc. Rev.* **42**, 4932 (2013).
9. M. Sarovar, A. Ishizaki, G. R. Fleming, K. B. Whaley, *Nature Physics* **6**, 462 (2010).
10. M. Karski, *et al.*, *Science* **325**, 174 (2009).
11. C. Weitenberg, *et al.*, *Nature* **471**, 319 (2011).
12. A. Peruzzo, *et al.*, *Science* **329**, 1500 (2010).
13. T. F. Gallagher, P. Pillet, *Advances in Atomic, Molecular, and Optical Physics*, A. et al, ed. (Academic Press, 2008), vol. 56 of *Advances In Atomic, Molecular, and Optical Physics*, pp. 161 – 218.
14. O. Mülken, *et al.*, *Phys. Rev. Lett.* **99**, 090601 (2007).
15. W. R. Anderson, J. R. Veale, T. F. Gallagher, *Phys. Rev. Lett.* **80**, 249 (1998).
16. I. Mourachko, *et al.*, *Phys. Rev. Lett.* **80**, 253 (1998).
17. W. R. Anderson, M. P. Robinson, J. D. D. Martin, T. F. Gallagher, *Phys. Rev. A* **65**, 063404 (2002).
18. J. Nipper, *et al.*, *Phys. Rev. Lett.* **108**, 113001 (2012).
19. S. Westermann, *et al.*, *Eur. Phys. J. D* **40**, 37 (2006).
20. C. S. E. van Ditzhuijzen, *et al.*, *Phys. Rev. Lett.* **100**, 243201 (2008).
21. A. Schwarzkopf, R. E. Sapiro, G. Raithel, *Phys. Rev. Lett.* **107**, 103001 (2011).

22. P. Schauß, *et al.*, *Nature* **491**, 87 (2012).

23. P. McQuillen, X. Zhang, T. Strickler, F. B. Dunning, T. C. Killian, *Phys. Rev. A* **87**, 013407 (2013).

24. G. Günter, *et al.*, *Phys. Rev. Lett.* **108**, 013002 (2012).

25. B. Olmos, W. Li, S. Hofferberth, I. Lesanovsky, *Phys. Rev. A* **84**, 041607 (2011).

26. J. D. Pritchard, *et al.*, *Phys. Rev. Lett.* **105**, 193603 (2010).

27. C. S. Hofmann, *et al.*, *Phys. Rev. Lett.* **110**, 203601 (2013).

28. T. Peyronel, *et al.*, *Nature* **488**, 57 (2012).

29. M. Fleischhauer, A. Imamoglu, J. P. Marangos, *Rev. Mod. Phys.* **77**, 633 (2005).

30. Materials and methods are available as supplementary material on *Science* online.

Acknowledgements We thank S. Wüster, T. Pohl, I. Bloch, M. Höning and M. Fleischhauer for fruitful discussions. This work is supported in part by the Heidelberg Center for Quantum Dynamics and by the Deutsche Forschungsgemeinschaft under WE2661/10.2. G.G. and C.S.H. acknowledge support by the Studienstiftung des deutschen Volkes, H.S. from the Landesgraduierten Akademie, M.R.D.S.V. (Grant No. FP7-PEOPLE-2011-IEF-300870) and S.W. (Grant No. PERG08-GA-2010-277017) from the EU Marie-Curie program, and V.G. from the EU Marie-Curie program ITN COHERENCE (Grant No. FP7-PEOPLE-2010-ITN-265031).

Supplementary Materials

Materials and Methods

Imaging experimental sequence

In the experiment we start with a cigar-shaped Gaussian cloud of ultracold ^{87}Rb atoms prepared in the state $|g = 5S_{1/2}, F = 2, m_F = 2\rangle$ (*1*). To demonstrate the imaging, we excite in a first step Rydberg impurities in state $|i = 50S\rangle$ in a small central region of the cloud using a focused, direct two-photon excitation. The excitation is two-photon resonant and 65 MHz detuned from the intermediate-state $|e = 5P_{3/2}, F = 3, m_F = 3\rangle$ as indicated in Fig. 1B. The peak atomic density is $\rho_0 = 2.4 \times 10^{11}\,\mathrm{cm}^{-3}$. The impurity excitation pulse is followed by the acquisition of the image under EIT-conditions using separate lasers. We employ an EIT-ladder system consisting of the states $|g\rangle$, $|e\rangle$ and $|p = 37S_{1/2}, m_J = 1/2\rangle$. The probe and coupling beams are counter-aligned and tuned to the single-photon resonances $|g\rangle \rightarrow |e\rangle$ and $|e\rangle \rightarrow |p\rangle$, respectively. The probe uniformly illuminates the cloud with typical Rabi-frequency $\sim 2\,$MHz. The probe light transmitted through the cloud is imaged onto a CCD camera with a resolution of $9\ \mu$m (Rayleigh criterion). The coupling beam is focused onto the atoms to an elongated Gaussian intensity profile with $\sigma_x = 64\,\mu$m and $\sigma_y = 10\,\mu$m, and $\Omega_c \sim 9\,$MHz. Under these conditions the probe photon density inside the medium is much smaller than the probe-blockade density and therefore effects of probe-probe interactions on EIT can be neglected (*2–5*). Typical exposure times for image acquisition are $t =$ 2-20 μs. For imaging we maximize the interstate blockade radius $R_{ip} = 3.8 \pm 0.3\,\mu$m via the Förster-resonance, however it is still slightly smaller than the impurity-impurity blockade radius $R_{ii} = 4.2 \pm 0.2\,\mu$m (including collective enhancement with approximately 73 atoms per blockade volume (*6*)). After the image, electric fields are switched to field ionize the impurities while preserving the probe rydberg state. The resulting ions are counted with an overall detection efficiency of 0.4 (*3*).

Image processing

To obtain the Rydberg distribution from the camera images one has to account for the residual absorption due to imperfect transparency and for the spatial inhomogeneity of the coupling beam. Therefore we take two images from different realizations of the experiment: one with impurities, and one without impurity excitation. The optical density of additional absorbers can then be calculated using the two images by $OD_{add} = -\log(I_{\mathrm{imp}}/I_{\mathrm{no\ imp}})$ where I denotes the transmitted intensities of the probe beam for the two images. To reduce the effects of shot-to-shot fluctuations in the atom number, photon-shot-noise and fringes, we construct an optimal image $I_{\mathrm{no\ imp,opt}}$ for each image with impurities (*7*). From OD_{add} we extract the number of additional two-level absorbers N_{add}.

Time integrated diffusion

Our images provide the time-integrated impurity distribution. Assuming an initial Gaussian distribution of impurities with width σ_0 and diffusive expansion, the horizontal distribution during imaging (with exposure time t_{EXP}) is given by

$$\frac{A_0}{\sqrt{2\pi}t_{\mathrm{EXP}}}\int_0^{t_{\mathrm{EXP}}}\frac{1}{\sqrt{2Dt+\sigma_0^2}}e^{-\frac{x^2}{2\left(2Dt+\sigma_0^2\right)}}\,\mathrm{dt}.$$

The second moment σ_x^2 of the time-integrated distribution is

$$\sigma_x^2 = \sigma_0^2 + Dt$$

which we fit to the data to extract the diffusion coefficient D.

Experimental conditions for excitation transport

The experiments on energy transport follow the same experimental sequence as the demonstration of imaging, except that the impurity state is changed to $|38S\rangle$.

For the transport experiment on the Förster resonance, the probe Rabi frequency is $\Omega_p = 2\pi \times (2.2 \pm 0.3)\,\mathrm{MHz}$, the coupling Rabi frequency is $\Omega_c = 2\pi \times (9 \pm 1)\,\mathrm{MHz}$, and the atomic density is $\rho_0 = (4.7 \pm 0.5) \times 10^{10}\,\mathrm{cm}^{-3}$. For the transport experiment away from the Förster resonance, we use : $\Omega_p = 2\pi \times (1.8 \pm 0.2)\,\mathrm{MHz}$, $\Omega_c = 2\pi \times (9 \pm 1)\,\mathrm{MHz}$, and $\rho_0 = (8.0 \pm 0.8) \times 10^{10}/\mathrm{cm}^3$.

Supplementary Text: Model of the transport dynamics

Dipolar energy transfer on the Förster resonance

We consider an impurity coupled to each of the neighbouring atoms by a dipole-dipole state-exchange interaction $V_{dd}(r) = C_3/r^3$. This term is responsible for a coherent excitation transfer to the probe atom dressed by the laser fields with frequency $\omega_{hop}(r) = 2V_{dd}(r)\rho_{pp}(r)$, where the population ρ_{pp} of the $|p\rangle$ state on the probe atom is affected by the presence of the impurity. The latter is also responsible for a finite population ρ_{ee} of the intermediate state, resulting in light scattering at a rate $\rho_{ee}\Gamma$.

To evaluate ρ_{pp} and ρ_{ee}, we assume stationary state for the laser-driven evolution of the probe atom. Throughout this Supplementary Information we use simplified expressions assuming the weak probe limit $\Omega_p \ll \Omega_c, \Gamma$. Neglecting laser linewidth and decay of the Rydberg state, we obtain:

$$\rho_{pp}(r) = \frac{\Omega_p^2\Omega_c^2}{\Omega_c^4 + 4V_{dd}(r)^2\Gamma^2}; \quad \rho_{ee}(r) = \frac{4V_{dd}(r)^2\Omega_p^2}{\Omega_c^4 + 4V_{dd}(r)^2\Gamma^2} \tag{2}$$

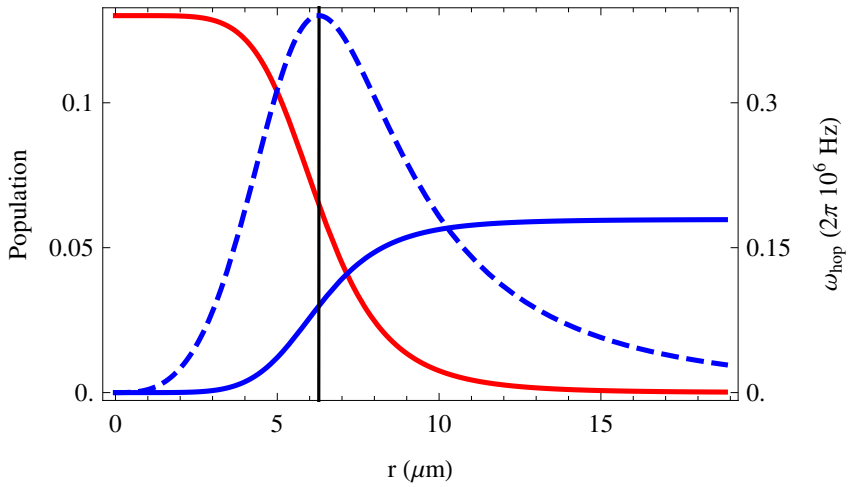

Figure S1: **Probe atom state as a function of distance to the impurity**. The continuous blue and red curves show the populations $\rho_{pp}(r)$ and $\rho_{ee}(r)$, respectively. The vertical line marks the blockade radius R_{ip}, at which the Rydberg state population is suppressed by a factor of two by the interactions. The dashed blue curve shows the hopping frequency $\omega_{hop}(r)$, which due to the low-distance suppression of the Rydberg population and the long-distance decay of the interaction presents a maximum approximately at R_{ip}. For parameters see Materials and Methods.

In Fig. S1 we show both these populations, from which two observations can be made. First, we observe that within a sphere of radius $\approx R_{ip} = (2\Gamma C_3/\Omega_c^2)^{1/3}$ the Rydberg population is highly suppressed. As a consequence, the hopping frequency $\omega_{hop}(r)$ presents a peaked maximum at approximately R_{ip}, responsible for a preferred hopping distance. Second, we observe that within the same sphere the atoms present a significant population of the intermediate state, and thus strongly scatter light.

The transport dynamics results from the coherent hopping process of the impurity to all of the neighbouring atoms, damped by the light scattering of the ensemble of atoms in the vicinity of the impurity, with rate $\gamma_{env} = \sum_{atoms} \rho_{ee}\Gamma$. If $\gamma_{env} \gg \omega_{hop}(r)$ at any distance, the excitation transfer to one probe atom behaves classically, with rate $\Gamma_{hop}(r) = \omega_{hop}(r)^2/\gamma_{env}$. This rate, falling off as $1/r^6$, can be spatially integrated in three dimensions to obtain the total hopping rate $\Gamma_{hop}^{tot} \simeq \Omega_p^2/2\Gamma$ and the mean square hop distance $r_{hop}^2 = \langle \vec{r}^2 \rangle \simeq 10/3 R_{ip}^2$. The diffusion coefficient in three dimensions $D = \langle \vec{r}^2 \rangle \Gamma_{hop}^{tot}/6$ then becomes:

$$D \simeq \frac{5}{18} R_{ip}^2 \frac{\Omega_p^2}{\Gamma} \tag{3}$$

From the parameters used in our experiment on the Förster resonance (see Material and Methods), and with $C_3 = 2\pi \times 1.6\,\mathrm{GHz}\,\mu\mathrm{m}^3$, we expect diffusion with $D = 55 \pm 23\,\mu\mathrm{m}^2/\mu\mathrm{s}$,

where the stated uncertainty is dominated by the calibration of Ω_p. We also estimate the amplification factor $A \simeq \gamma_{env}\Gamma/\Omega_p^2 = 77 \pm 25$.

Van der Waals energy transfer away from the Förster resonance

In the case of a van der Waals exchange interaction, the expressions for γ_{env} and Γ_{hop} do not present a simple analytical form. Instead we use a hard sphere approximation with radius $R_{vdw} = (2\Gamma C_6/\Omega_c^2)^{1/6}$: for $r < R_{vdw}$ we set $\rho_{ee} \simeq \Omega_p^2/\Gamma^2$ and $\rho_{pp} \simeq 0$, while for $r \geq R_{vdw}$ we set $\rho_{ee} \simeq 0$ and $\rho_{pp} \simeq \Omega_p^2/\Omega_c^2$. Considering that ω_{hop} decays with $1/r^6$, we get after 3D spatial integration $\Gamma_{hop}^{tot} \simeq \Omega_p^2/3\Gamma$ and $r_{hop} \simeq \sqrt{9/7}R_{vdw}$. Consequently, we again obtain a simple expression for the diffusion coefficient :

$$D \simeq \frac{1}{14} R_{vdw}^2 \frac{\Omega_p^2}{\Gamma} \tag{4}$$

The differences as compared to the dipolar exchange are the numerical pre-factor and the strongly reduced blockade radius. In the presence of a Förster defect δ_F, these are related by $R_{vdw}/R_{ip} = \left(\frac{\Omega_c^2}{4\Gamma\delta_F}\right)^{1/6} \approx 0.6$ for our parameters.

From the parameters used in our experiment away from the Förster resonance (see Material and Methods), and with $\delta_F = 2\pi \times 100\,\mathrm{MHz}$, we expect diffusion with coefficient $D = 3.0 \pm 0.9\,\mu\mathrm{m}^2/\mu\mathrm{s}$ and amplification $A = 14 \pm 3$. Note that the direct numerical integration of γ_{env} and Γ_{hop} without hard sphere approximation gives a similar value $D = 2.2\,\mu\mathrm{m}^2/\mu\mathrm{s}$.

References and Notes

1. C. S. Hofmann, *et al.*, *arXiv:1307.1074* (2013).

2. J. D. Pritchard, *et al.*, *Phys. Rev. Lett.* **105**, 193603 (2010).

3. C. S. Hofmann, *et al.*, *Phys. Rev. Lett.* **110**, 203601 (2013).

4. T. Peyronel, *et al.*, *Nature* **488**, 57 (2012).

5. D. Petrosyan, J. Otterbach, M. Fleischhauer, *Phys. Rev. Lett.* **107**, 213601 (2011).

6. R. Löw, *et al.*, *Journal of Physics B: Atomic, Molecular and Optical Physics* **45**, 113001 (2012).

7. C. F. Ockeloen, A. F. Tauschinsky, R. J. C. Spreeuw, S. Whitlock, *Phys. Rev. A* **82**, 061606 (2010).